Tension is required but not sufficient for focal adhesion maturation without a stress fiber template

Patrick W. Oakes,[1,2,3] Yvonne Beckham,[1,3] Jonathan Stricker,[1,2,3] and Margaret L. Gardel[1,2,3]

[1]Institute for Biophysical Dynamics, [2]Department of Physics, and [3]The James Franck Institute, University of Chicago, Chicago, IL 60637

Focal adhesion composition and size are modulated in a myosin II–dependent maturation process that controls adhesion, migration, and matrix remodeling. As myosin II activity drives stress fiber assembly and enhanced tension at adhesions simultaneously, the extent to which adhesion maturation is driven by tension or altered actin architecture is unknown. We show that perturbations to formin and α-actinin 1 activity selectively inhibited stress fiber assembly at adhesions but retained a contractile lamella that generated large tension on adhesions. Despite relatively unperturbed adhesion dynamics and force transmission, impaired stress fiber assembly impeded focal adhesion compositional maturation and fibronectin remodeling. Finally, we show that compositional maturation of focal adhesions could occur even when myosin II–dependent cellular tension was reduced by 80%. We propose that stress fiber assembly at the adhesion site serves as a structural template that facilitates adhesion maturation over a wide range of tensions. This work identifies the essential role of lamellar actin architecture in adhesion maturation.

Introduction

Focal adhesions integrate mechanical, biochemical, and structural cues to provide dynamic links between the actin cytoskeleton and the surrounding ECM that are essential in guiding cell differentiation, proliferation, migration, and ECM remodeling (Vogel and Sheetz, 2006; Geiger et al., 2009; Parsons et al., 2010; Schwartz, 2010; Geiger and Yamada, 2011). Understanding how focal adhesions sense varied cues to modulate downstream signaling networks and cell–ECM force transmission is critical to elucidating the sensory mechanisms underlying diverse cellular processes. However, because cytoskeletal biochemistry, force generation, and organization are dynamically interwoven, identifying functional dependencies of these inputs on focal adhesion signaling has proven challenging.

Myosin II mediates a maturation of focal adhesions whereby morphological and compositional changes occur to modulate adhesion dynamics, traction forces on the ECM, and ECM remodeling (Riveline et al., 2001; Webb et al., 2004; Gardel et al., 2010; Geiger and Yamada, 2011). During myosin-mediated maturation, enhanced tension occurs concomitantly with the assembly of a stress fiber at the adhesion in a Dia1-dependent fashion (Chrzanowska-Wodnicka and Burridge, 1996; Amano et al., 1997; Riveline et al., 2001; Hotulainen and Lappalainen, 2006). Comprised of actin filaments bundled with alternating bands of α-actinin and myosin, these dorsal or radial stress fibers (RSFs) connect focal adhesions to the lamellar actin cytoskeleton and are thought to be important for transmission of myosin-generated forces across the cell and to the focal adhesions (Chrzanowska-Wodnicka and Burridge, 1996; Peterson et al., 2004; Hotulainen and Lappalainen, 2006). Because changes in tension at the adhesion plaque occur simultaneously with stress fiber assembly, the relative contributions of mechanical cues and changes in the lamellar actin architecture to myosin-mediated focal adhesion maturation are unknown. Although focal adhesion maturation is widely presumed to be a force-dependent process (Vogel and Sheetz, 2006; Geiger et al., 2009; Parsons et al., 2010; Schwartz, 2010; Geiger and Yamada, 2011), recent evidence suggests that lamellar actin organization may also be important (Choi et al., 2008).

Here, we distinguish between the roles of tension and lamellar actin architecture in focal adhesion maturation by examining focal adhesions formed in cells where RSF assembly at adhesions is selectively impaired by formin inhibition (Dia Inh)

P.W. Oakes and Y. Beckham contributed equally to this paper.

Correspondence to Margaret L. Gardel: gardel@uchicago.edu

Abbreviations used in this paper: GAPDH, glyceraldehyde 3-phosphate dehydrogenase; KD, knockdown; MLC, myosin light chain; PAA, polyacrylamide; RSF, radial stress fiber; shRNA, short hairpin RNA; TIRF, total internal reflection fluorescence; WT, wild type.

The Rockefeller University Press $30.00
J. Cell Biol. Vol. 196 No. 3 363–374
www.jcb.org/cgi/doi/10.1083/jcb.201107042

or reduced expression of α-actinin 1 (Atn-1 knockdown [KD]). In Dia Inh and Atn-1 KD cells, myosin activity within the lamella drives a rapid retrograde flow of transverse arcs that generate large tension on focal adhesions. Despite unperturbed adhesion dynamics and force transmission, canonical hallmarks of focal adhesion maturation are not observed. In the absence of RSF assembly, the focal adhesion length is smaller, the accumulation of phosphorylated paxillin (Pxn) and FAK in adhesions is markedly reduced, and the formation of tensin-rich fibrillar adhesions required for fibronectin remodeling is suppressed. Thus, critical aspects of focal adhesion maturation are not driven by mechanotransduction pathways alone and require the assembly of a stress fiber at the adhesion plaque. Finally, we show that focal adhesion compositional maturation and matrix remodeling occur even when myosin-dependent cellular tension is reduced by 80%. Together, these results demonstrate that a nominal threshold of myosin-dependent tension is required, but not sufficient, to drive focal adhesion maturation. Rather, the lamellar actin density at the focal adhesion plaque is crucial. We propose that the local accumulation of F-actin in the form of a dense stress fiber template at the focal adhesion plaque facilitates the recruitment and stable association of focal adhesion proteins required for their compositional maturation. Our data identify the important role of lamellar actin architecture in focal adhesion maturation.

Results

RSF assembly requires Dia and Atn-1

Across a broad spectrum of contractile cells in culture, stress fibers are a prominent feature of the lamellar actin cytoskeleton. Characterized by alternating bands of α-actinin and myosin (Peterson et al., 2004; Hotulainen and Lappalainen, 2006), the actomyosin organization within stress fibers is reminiscent of sarcomeres in striated muscle and suggests an important role in the transmission of myosin II forces across the cell. In human osteosarcoma (U2OS) cells, distinct populations of stress fibers can be readily identified by their orientation with respect to the cell edge and actin assembly mechanisms (Hotulainen and Lappalainen, 2006). Transverse arcs are contractile bundles of actin that form parallel to the cell edge (Fig. 1 A, red arrows) by the myosin-mediated annealing of lamellipodial F-actin (Heath, 1983; Forscher and Smith, 1988; Hotulainen and Lappalainen, 2006; Koestler et al., 2008; Burnette et al., 2011). Transverse arcs can be distinguished from other stress fibers, despite a similar composition of bundled filaments, in that they are highly dynamic structures, undergoing rapid contraction and flow toward the center of the cell, and they lack focal adhesions at their ends. Another distinct subset of stress fibers form via Dia1-mediated actin assembly at focal adhesions, are integrated with transverse arcs along their length, and are oriented perpendicular to the cell edge (Figs. 1 A [yellow arrows], S1, and S3; Hotulainen and Lappalainen, 2006). Because of their orientation within the cell, we refer to these as RSFs; these are identical to previously described dorsal stress fibers (Hotulainen and Lappalainen, 2006). Over 95% of wild-type (WT) U2OS cells contain RSFs that occur approximately every 6.25 µm along the cell edge (Fig. 1, B and C). To compare the relative density of F-actin within different regions of the lamella, we quantified the intensity of fluorescent phalloidin images and found that the density of F-actin within RSFs was ∼30% greater than in the transverse arcs (Fig. 1 D). Because of their presumed role in regulating force transmission to focal adhesions, we wished to explore the consequences of inhibiting RSF assembly on focal adhesion maturation and cell–ECM force transmission.

It has been previously shown that RSF assembly in U2OS cells is suppressed by reduced expression of the formin Dia1 (Hotulainen and Lappalainen, 2006). Here, we chose to take advantage of the recently identified formin inhibitor SMIFH2 (Rizvi et al., 2009) to inhibit formin-mediated actin assembly. After incubation with 15 µM SMIFH2 for >4 h, only 40% of U2OS cells displayed RSFs (Dia Inh in Fig. 1 A; Figs. S2 and S3). Approximately 40% of the cells contained transverse arcs only, and the remaining 20% of cells contained no prominent actin bundles within the lamella (Figs. 1 B and S3). In the Dia-inhibited cells containing RSFs, the mean density of RSFs was reduced by 50% (Fig. 1 C), and the overall density of F-actin within RSFs was reduced by ∼30–40% (Fig. 1 D). This reduction in RSF assembly presumably reflects the role of formins as nucleators of lamellar actin at focal adhesion sites (Gupton et al., 2007; Campellone and Welch, 2010). To confirm that our results with the Dia Inh were primarily a result of effects of Dia1 inhibition, we used siRNA to reduce expression of Dia1. In siRNA Dia1 cells, we observed a larger fraction of cells that still contained some RSFs (∼70%; Figs. 1 B and S3), but both the RSF density within cells and the amount of F-actin within RSFs were reduced to similar extents, as found with the inhibitor, with no statistical difference between these populations (Fig. 1, C and D). Thus, we conclude that the Dia inhibitor is significantly impacting Dia1 at this concentration. Interestingly, with both treatments, we also observed a significant decrease in the density of F-actin found within transverse arcs (∼30%; Fig. 1 D), indicating a prominent role of Dia1 as a nucleator of lamellar actin.

Because of the known role of Atn-1 in focal adhesion maturation (Laukaitis et al., 2001; Choi et al., 2008) and its prominent localization to RSFs (Fig. S1), we hypothesized that Atn-1 might also be important to RSF assembly. Strikingly, when we reduced the expression of Atn-1 by 65% via short hairpin RNA (shRNA; Atn-1 KD), <60% of the cells displayed RSFs, with the remaining cells displaying either transverse arcs only (∼30%) or no bundles at all (10%; Figs. 1 [A and B], S2, and S3). Within the cells displaying RSFs, the linear density of stress fibers decreased to 0.06 RSF per µm, and the density of F-actin within these RSFs was reduced by 30%, as compared with RSFs in control cells (Fig. 1, C and D). Thus, Atn-1 cross-linking of F-actin plays a crucial role in the formation of RSFs, consistent with a previous finding (Choi et al., 2008).

Retrograde flow is enhanced in contractile lamellar networks depleted of RSFs

To explore the extent to which the organization of active myosin II within the lamella was affected by the inhibition of RSF assembly, we visualized the enzymatically active fraction of

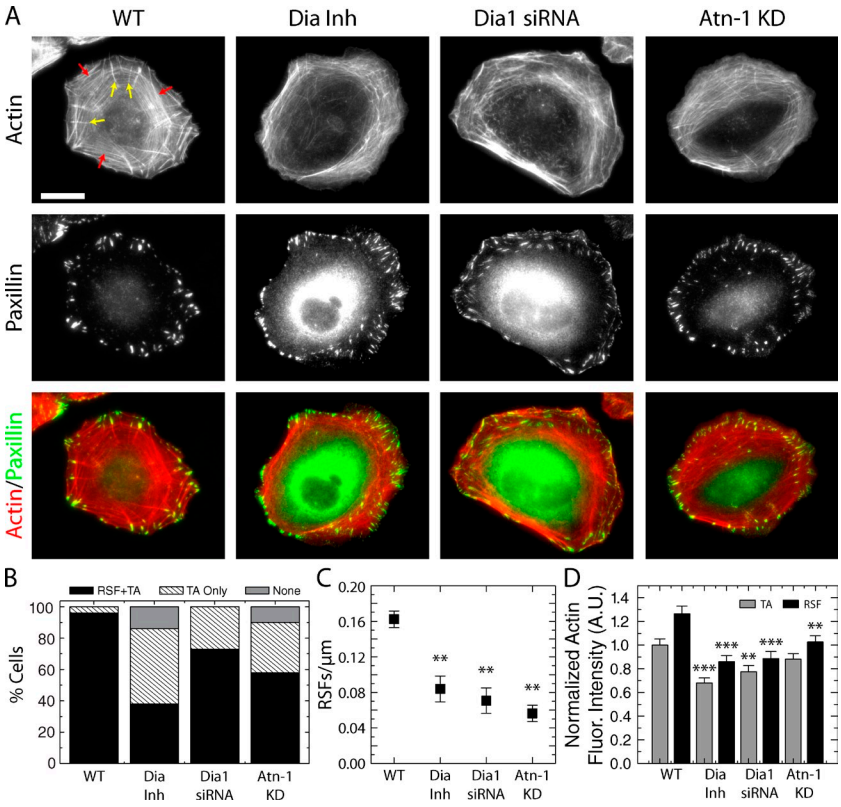

Figure 1. **RSF formation is suppressed through formin inhibition or reduced expression of Dia1 or Atn-1.** (A) Images of F-actin visualized by fluorescent phalloidin (top row) and Pxn immunofluorescence (middle row) are shown for WT U2OS cells, cells treated with 15 μM of the formin inhibitor SMIFH2 (Dia Inh), cells with reduced expression of Dia1 via siRNA (Dia1 siRNA), and cells with reduced expression of Atn-1 by shRNA (Atn-1 KD). Yellow arrows indicate RSFs, and red arrows indicate transverse arcs in the WT cells. Bar, 20 μm. (B) Percentages of cells containing both RSFs and transverse arcs (RSF + TA), transverse arcs only (TA Only), or no actin bundles (None) were determined for the WT, Dia Inh, Dia1 siRNA, and Atn-1 KD cells, as described above (n = 49, 50, 22, and 50 for the four conditions, respectively). Representative images from each classification of cells can be seen in Fig. S3. (C) Mean linear density of RSFs, measured as the number of RSFs per micrometer along the cell edge for each of the four conditions (error bars indicate SEM; n = at least 10 cells containing five to six RSFs; **, P < 0.01 with respect to WT). (D) Mean background-corrected fluorescence (Fluor.) intensity of fluorescent phalloidin staining of F-actin in transverse arcs and RSFs for each condition, normalized to the transverse arcs in WT cells (error bars indicate SEM; n = 20 regions from 10 cells for each condition; **, P < 0.01; ***, P < 0.001 with respect to WT). A.U., arbitrary unit.

myosin II by immunofluorescence of myosin light chain (MLC) phosphorylated at serine 19 (pMLC; Adelstein and Conti, 1975) while also visualizing the F-actin cytoskeleton with fluorescent phalloidin (Fig. 2 A). In all populations, active myosin localized throughout the lamella primarily along transverse arcs (Fig. 2 A). We tested cell lysates for relative amounts of pMLC and total MLC via Western blotting (Fig. 2 B) and used densitometry to quantify the ratio of pMLC to MLC (Fig. 2 C). We found small reductions in the amount of MLC and pMLC but found no significant difference in the ratio of pMLC to MLC in both Dia-inhibited and Atn-1 KD cells. We speculate that this small reduction in active myosin may be a result of changes in biochemical signaling to Rho pathways caused by changes in lamellar organization or focal adhesions (Schwartz, 2010), but a definitive understanding would require further study.

Importantly, both of these methods provide a means to disrupt RSF assembly without directly impacting myosin II activity. As such, these systems are uniquely suited to determine the roles of lamellar actin architecture in force transmission and focal adhesion maturation. To assess the consequences of these perturbations on myosin-dependent retrograde flow of lamellar actin, we transfected cells with GFP-actin and used quantitative image analysis to track the rate and direction of movement of the actin network in a series of time-lapse images (Danuser and Waterman-Storer, 2006). Consistent with previous studies, lamellar actin in WT U2OS cells underwent retrograde flow at ~5 nm/s (Hotulainen and Lappalainen, 2006; Aratyn-Schaus and Gardel, 2010; Aratyn-Schaus et al., 2011), which is identical to the rate of RSF elongation at focal adhesions (Hotulainen and Lappalainen, 2006).

Retrograde flow of actin was also observed in both Dia-inhibited and Atn-1 KD cells. In Atn-1 KD cells, a network of dim transverse arcs assembled at the lamellipodia base and underwent contraction and retrograde movement (Fig. 2 [D and F] and Video 1). A small fraction of the faint transverse arcs appeared to get stuck at adhesion sites and reoriented to become perpendicular to the cell edge (Fig. 2 E), but these bundles failed to elongate at the adhesion site or intensify, as during RSF assembly. Moreover, the lamellar retrograde flow in both the Dia-inhibited cells and the Atn-1 KD cells increased to ~10 nm/s, twice that of the WT cells (Fig. 2, F and G). The speed of myosin-dependent retrograde flow of lamellar actin is determined by the balance of myosin-driven tension to the sum of the lamellar viscoelastic resistance and friction sustained at focal adhesions (Rubinstein et al., 2009; Aratyn-Schaus and Gardel, 2010). The enhanced flow rate observed in lamella with impaired RSF assembly suggests that stress fibers within the contractile network may either provide more internal resistance to lamellar contraction or transmit more tension to focal adhesions.

RSFs are not necessary for force transmission to the ECM at focal adhesions

Because of their apparent structural function of connecting the lamellar actin to focal adhesions, RSFs are presumed to play an important role in force transmission to the ECM at focal adhesions. To clarify this role, we used traction force microscopy to measure the stress exerted by cells on the ECM at adhesions. In brief, cells expressing GFP-actin were plated on fibronectin-coated polyacrylamide (PAA) substrates suitable for traction force microscopy

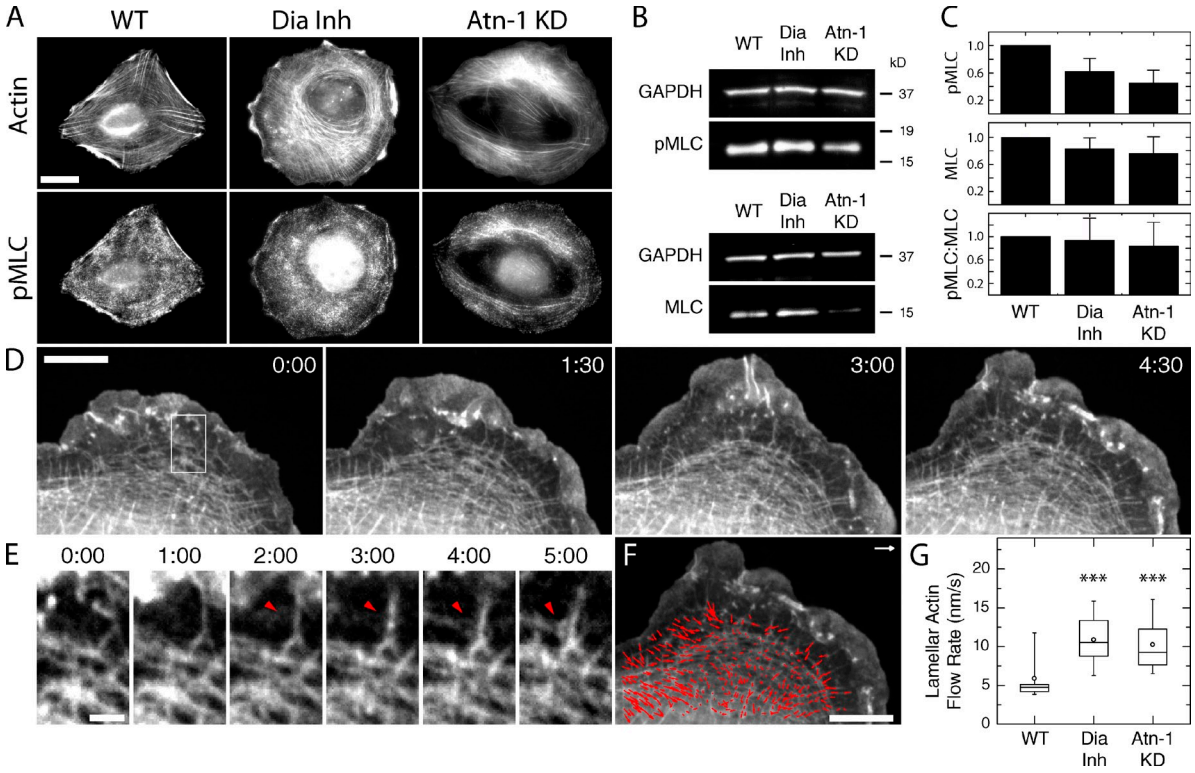

Figure 2. **Suppressing RSF assembly reduces the quantity of active myosin II but increases lamellar actin retrograde flow rate.** (A) Immunofluorescence images of pMLC and fluorescent phalloidin staining of F-actin are shown for WT, Dia Inh, and Atn-1 KD U2OS cells. Bar, 20 µm. (B) Western blots showing MLC and pMLC for each condition in relation to a glyceraldehyde 3-phosphate dehydrogenase (GAPDH) loading control. (C) Densitometry analysis of Western blots showing the relative levels of pMLC, MLC, and the ratio of pMLC to MLC for each condition, normalized to WT cells. There is no significant difference in the ratio of MLC to pMLC for each condition. The bar plot shows the mean ratio relative to WT cells (error bars indicate SEM; $n = 6$ for each condition). (D) A series of images of GFP-actin expressed in a protruding Atn-1 KD cell over time. Time is indicated in minutes/seconds. Bar, 10 µm. See Video 1. (E) Magnified images of the boxed region indicated at time 0 in D, illustrating the reorientation of a transverse arc to align in the direction of retrograde flow (red arrowheads). Bar, 2 µm. (F) Actin flow vectors are overlaid on the GFP-actin image from E at 4 min and 30 s. The white arrow represents 15 nm/s. Bar, 10 µm. (G) A box plot of the lamellar retrograde flow speed for each condition described (open circle = mean; box = 25th, 50th, and 75th percentile; whiskers = 5th and 95th percentile; $n > 150$ flow vectors from multiple regions in three to five cells for each condition; ***, $P < 0.001$ with respect to WT).

and analysis (Sabass et al., 2008). As previously observed in control U2OS cells (Aratyn-Schaus et al., 2011; Stricker et al., 2011), large traction stresses along the cell's periphery were observed (Fig. 3 A), and the mean total force generated by individual cells was 250 nN (Fig. 3 B).

Although the spatial distribution of traction forces was unchanged in both Dia-inhibited and Atn-1 KD cells, the magnitude of the traction stresses was impacted. Strikingly, the Atn-1 KD cells exerted ~40% more traction force on the substrate than WT cells (Fig. 3 B). In contrast, the myosin-dependent traction stress exerted in formin-inhibited or siRNA Dia1 cells was reduced by 60 or 35%, respectively (Fig. 3 B), but was still at least fourfold larger than the myosin-independent traction force generated by adherent U2OS cells (~25 nN; Aratyn-Schaus et al., 2011). The difference between the Dia Inh and Dia1 siRNA–treated cells is likely a result of the broad spectrum of formins inhibited by SMIFH2, including Dia2, but will require further study. The differences between the

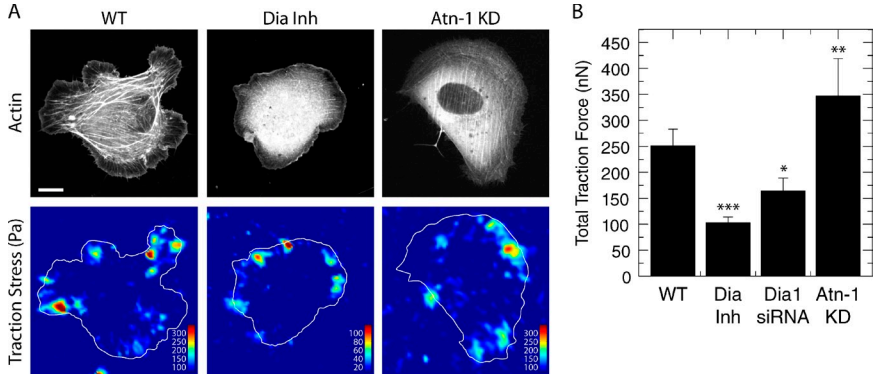

Figure 3. **Cells lacking RSFs generate large traction stresses.** (A) Images of GFP-actin (top row) and heat map of traction stress magnitude (bottom row) of WT, Dia Inh, and Atn-1 KD U2OS cells plated on fibronectin-coated PAA gels. For traction stress images, the white line indicates the cell outline, and the heat scale of traction stress (in Pa) is indicated at the bottom right. Bar, 10 µm. (B) Plot of the total traction force exerted by WT, Dia-inhibited, Dia1 siRNA, and Atn-1 KD U2OS cells (error bars indicate SEM; $n = 18, 14, 11$, and 24 cells for each condition, respectively; *, $P < 0.05$; **, $P < 0.01$; ***, $P < 0.001$ with respect to WT).

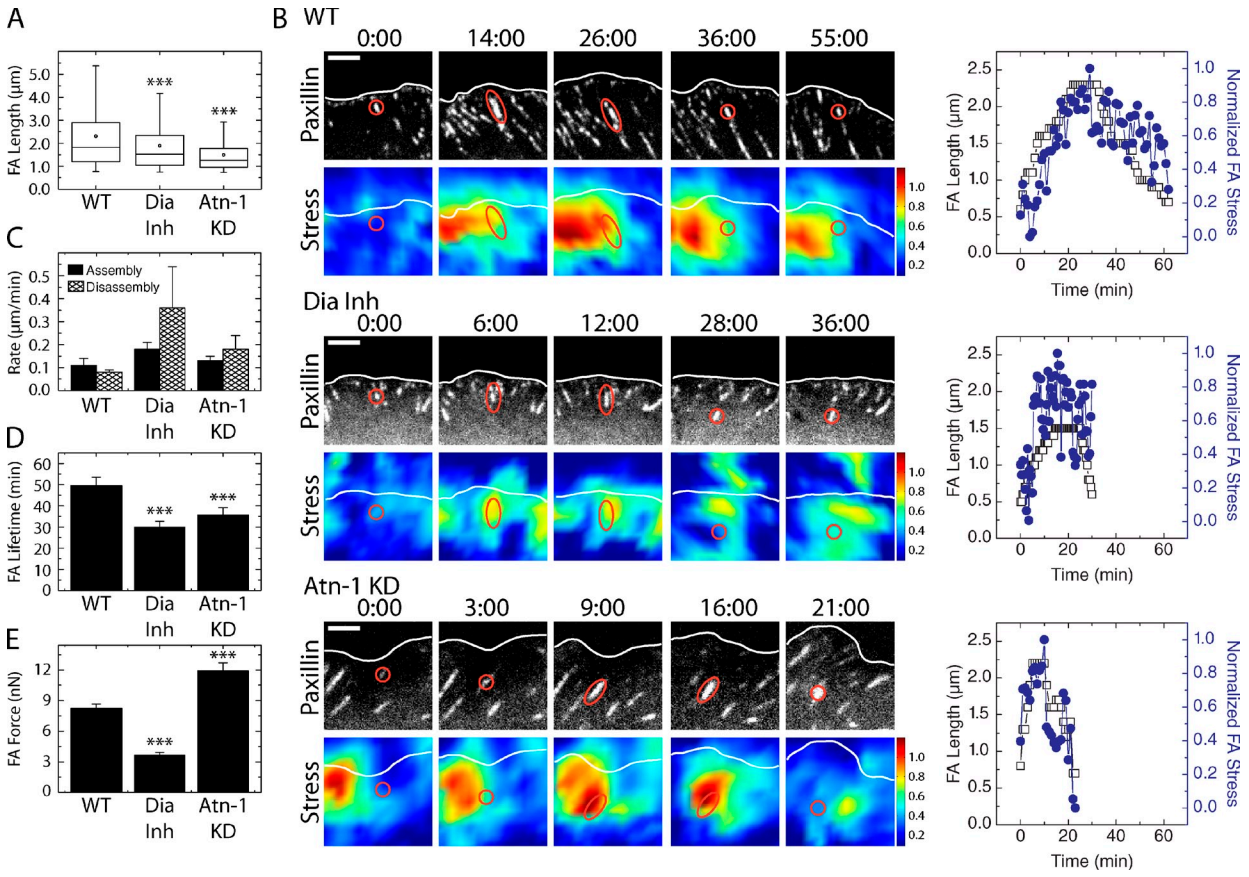

Figure 4. **Substantial tension is built up at focal adhesions despite impaired RSF assembly.** (A) Box plots of focal adhesion (FA) lengths of WT, Dia Inh, and Atn-1 KD U2OS cells (open circle = mean; box = 25th, 50th, and 75th percentile; whiskers = 5th and 95th percentile; n > 1,000 from 10 cells for each condition; ***, P < 0.001 with respect to WT). (B) Time series of GFP-Pxn and traction stress heat map images for representative WT, Dia-inhibited, and Atn-1 KD cells, showing the assembly and disassembly of a representative single focal adhesion and changes in traction stress. Bars, 3 μm. Focal adhesion length and normalized traction stress at the focal adhesion indicated by the red ovals are shown on the right. (C) Bar graph of the mean rates of focal adhesion assembly and disassembly for each of three conditions (error bars indicate SEM; n = 10 adhesions from two cells for each condition). (D) Bar graph of the mean focal adhesion lifetime (error bars indicate SEM; n = 26, 24, and 22 from two WT, Dia Inh, and Atn-1 KD cells, respectively; ***, P < 0.001 with respect to WT). (E) Plot of the mean traction stress exerted at individual focal adhesions (error bars indicate SEM; n = 51, 69, and 29 focal adhesions from three cells for WT, Dia-inhibited, and Atn-1 KD U2OS cells, respectively; ***, P < 0.001 with respect to WT).

formin-inhibited cells and the Atn-1 KDs indicate different roles of the proteins in force transmission within transverse arcs. Importantly, these data show that RSFs are not required for transmission of significant levels of myosin-generated stresses to the ECM at focal adhesions. Transverse arcs are sufficient to generate contractile stresses that can be efficiently transmitted to focal adhesions.

Force-mediated stabilization of focal adhesions occurs despite impaired RSF assembly

During myosin-mediated focal adhesion maturation, adhesion growth occurs concomitantly with RSF formation (Choi et al., 2008). Consequently, suppressing RSF assembly at adhesions reduces the size of focal adhesions (Riveline et al., 2001; Choi et al., 2008). Consistent with these results, immunofluorescence images of Pxn revealed that the mean length of focal adhesions was reduced by 20% in formin-inhibited cells and 40% in Atn-1 KD cells (Fig. 4 A), suggesting potential consequences to the traction force and morphological changes typically observed during focal adhesion assembly and disassembly.

To visualize the dynamics of focal adhesions with the local traction stress simultaneously, time-lapse images of GFP-Pxn expressed in cells plated on traction force substrates were obtained. Focal adhesion assembly in WT cells was characterized by the appearance of a submicrometer punctum of GFP-Pxn, which elongated at a rate of 0.1 μm/min to a final size of several micrometers (Fig. 4 [B and C] and Video 2). Elongated focal adhesions remained stable for ∼10 min and then disassembled at a similar rate of ∼0.1 μm/min (Fig. 4 [B and C] and Video 2). Overall, the mean adhesion lifetime in WT cells was 50 min (Fig. 4 D). During adhesion elongation, the local traction stress exerted on the substrate also increased, with mature adhesions sustaining a mean of ∼7.5 nN of force (Fig. 4 E).

Surprisingly, inhibition of RSF assembly did not impair tension buildup during focal adhesion assembly and growth. The rate of focal adhesion growth was enhanced by 20–50% in both formin-inhibited and Atn-1 KD cells, and focal adhesion

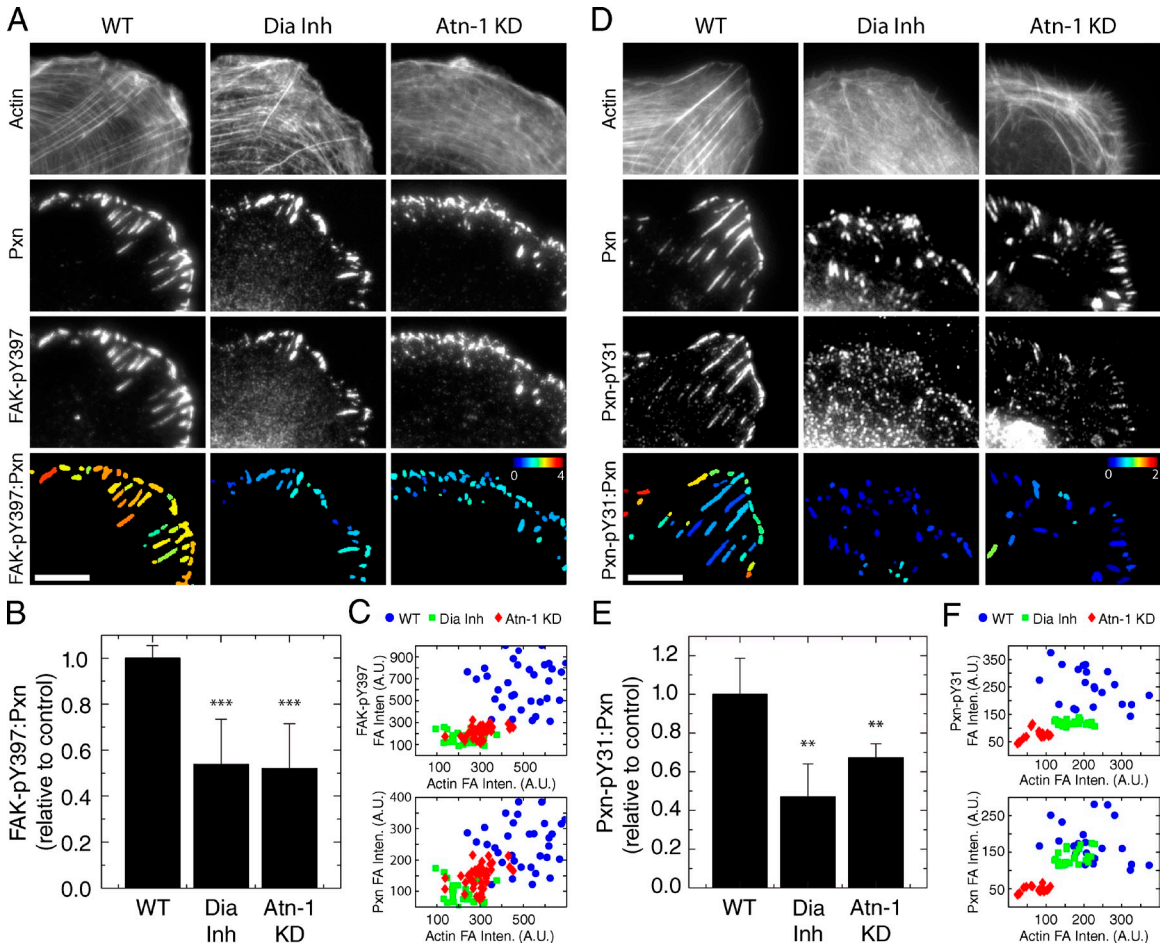

Figure 5. **Reduced accumulation of phosphorylated FAK and Pxn in focal adhesions of cells with impaired RSF assembly.** (A) Immunolocalization of F-actin, Pxn, and phosphorylated FAK (FAK-pY397) in representative WT, Dia Inh, and Atn-1 KD U2OS cells. The bottom row shows images representing the ratio of background-subtracted ratio intensity of FAK-pY397 to Pxn at individual focal adhesions in each of the three conditions. The range of the ratio is indicated by the bottom-right scale (in arbitrary units). Bar, 5 µm. (B) Bar graph of the mean ratio of FAK-pY397:Pxn, normalized to the WT cells (error bars indicate SEM; n > 1,000 focal adhesions from 10 cells for each condition; ***, $P < 0.001$ with respect to WT). (C) The mean intensity (Inten.) of FAK-pY397 or Pxn plotted against the mean intensity of actin at each focal adhesion (FA) for the focal adhesions shown in the bottom row of A. A.U., arbitrary unit. (D) Immunolocalization of actin, Pxn, and phosphorylated Pxn (Pxn-pY31) for each condition. The bottom row of images indicates the ratio of Pxn-pY31 to Pxn for each condition described. The range of the ratio is indicated by the bottom-right scale (in arbitrary units). Bar, 5 µm. (E) Bar graph of the mean ratio of Pxn-pY31:Pxn, normalized to the WT cells (error bars indicate SEM; n > 700 focal adhesions from six cells for each condition; **, $P < 0.01$ with respect to WT). (F) The mean intensity of Pxn-pY31 or Pxn plotted against the mean intensity of actin at each focal adhesion for the focal adhesions shown in the bottom row of D.

elongation coincided with an increase in traction stress (Fig. 4 [B and C] and Video 2). The tension sustained at elongated focal adhesions reflected the same trend observed across entire cells, with the mean force sustained by adhesions in formin-inhibited cells reduced to ∼3 nN and that sustained by adhesions in Atn-1 KD cells increased to ∼12 nN (Fig. 4 E). Importantly, the tension sustained at adhesion plaques for each condition was significantly higher than the 0.9-nN tension we previously determined was necessary to stabilize and promote adhesion growth (Aratyn-Schaus and Gardel, 2010).

Thus, RSFs are not necessary for focal adhesions to experience large forces over time scales characteristic of myosin-mediated focal adhesion maturation (Webb et al., 2004). However, we did find that the lifetime of adhesions in both formin-inhibited and Atn-1 KD cell lines was reduced to ∼30 min (Fig. 4 D). These data indicate that RSFs may be responsible for stabilizing adhesions over long times and slowing their disassembly.

Adhesions formed by transverse arcs have reduced levels of phosphorylated Pxn and FAK

During focal adhesion assembly, focal adhesion size and tension on the adhesion plaque increase concomitantly (Riveline et al., 2001; Stricker et al., 2011). Here, we found that inhibiting RSF assembly reduced the focal adhesion size but did not impair the tension sustained at focal adhesions. To assess how inhibition of RSF assembly affected other metrics of focal adhesion maturation, we sought to determine the extent of canonical posttranslational modifications to focal adhesion–signaling proteins characteristic of myosin-mediated maturation. During myosin-mediated focal adhesion maturation, FAK is recruited to adhesion plaques, undergoes autophosphorylation at tyrosine 397 (FAK-pY397), and then mediates the phosphorylation of Pxn at numerous sites, including tyrosine 31 (Pxn-pY31; Webb et al., 2004; Ballestrem et al., 2006;

Zaidel-Bar et al., 2007). Cells were fixed and immunostained for Pxn and either phosphorylated FAK (FAK-pY397) or phosphorylated Pxn (Pxn-pY31; Fig. 5). To compare the extent of Pxn and FAK phosphorylation between the three conditions, we used quantitative image analysis to calculate the ratio of FAK-pY397:Pxn and Pxn-pY31:Pxn (Fig. 5, A, B, D, and E). The level of FAK-pY397 was reduced to 50% that of control cells for both perturbations to formin activity and Atn-1 expression (Fig. 5 B). This is consistent with a reduction in the overall amount of integrin-mediated signaling to FAK, as is found in nascent adhesions (Shi and Boettiger, 2003). The levels of pY31-Pxn were reduced to ∼45 and 60% that of control for the Dia Inh and Atn-1 KD cells, respectively (Fig. 5 E), and are comparable with the levels observed in nascent adhesions (Zaidel-Bar et al., 2007; Pasapera et al., 2010). The reduction of FAK-pY397 and Pxn-pY31 in Dia Inh and Atn-1 KD cells was confirmed with Western blot analysis of whole-cell lysates (Fig. S4, A–C). Therefore, despite the high tension sustained at focal adhesions, the loss of RSFs resulted in a reduced amount of tyrosine phosphorylation to key focal adhesion proteins that are prominent signatures of myosin-mediated adhesion maturation. Although these posttranslational modifications are widely presumed to occur as a consequence of myosin-generated tension (Geiger et al., 2009; Gardel et al., 2010; Parsons et al., 2010), our data show that tension, in the absence of stress fiber architecture, is not sufficient to promote these classical hallmarks of focal adhesion signaling in U2OS cells. Consistent with this hypothesis, we observed a strong correlation between the actin density at the focal adhesion plaque and the density of Pxn, pY31-Pxn, and pY397-FAK (Fig. 5, C and F). The reduced F-actin density observed at focal adhesions in Dia-inhibited or Atn-1 KD cells is concomitant with reduced density of focal adhesion proteins.

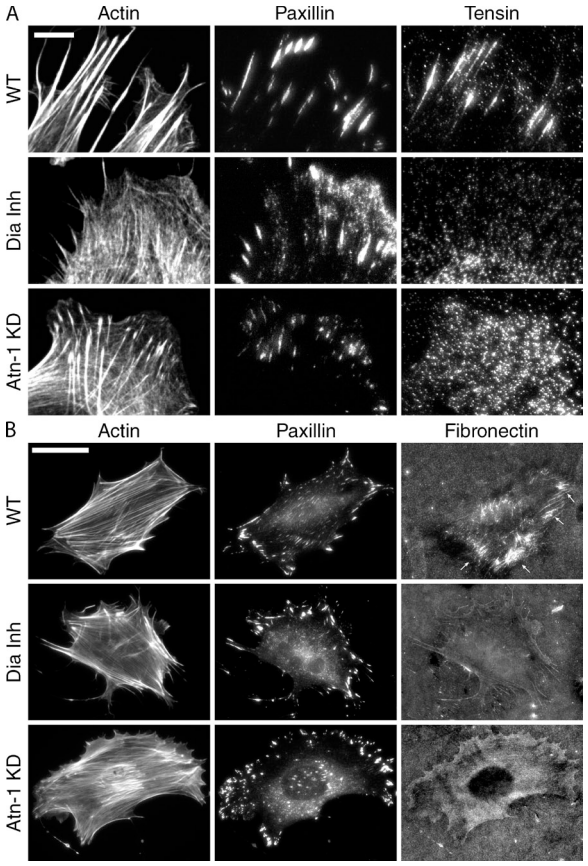

Figure 6. **The maturation of focal adhesions into tensin-rich fibrillar adhesions is abrogated in the absence of RSFs.** (A) Representative immunofluorescence TIRF images of Pxn and tensin along with the corresponding confocal actin image for WT, Dia Inh, and Atn-1 KD fibroblasts on fibronectin-coated glass coverslips. Bar, 10 µm. (B) Representative immunofluorescence actin, Pxn, and fibronectin images for WT, Dia-inhibited, and Atn-1 KD fibroblasts on fibronectin-coated glass coverslips 24 h after plating. The arrows indicate representative areas of fibronectin remodeling. Bar, 50 µm.

Cells with impaired RSF assembly are unable to remodel ECM

In fibroblasts, focal adhesion maturation culminates in the formation of tensin-rich fibrillar adhesions, which are essential for fibronectin matrix remodeling (Pankov et al., 2000; Zaidel-Bar et al., 2007; Geiger and Yamada, 2011). To explore the physiological consequences of impaired focal adhesion maturation in cells with reduced stress fiber assembly at focal adhesions, we inhibited formin and reduced expression of Atn-1 in NIH 3T3 fibroblasts. Although the organization of stress fibers in NIH 3T3 fibroblasts precludes identification of RSFs from transverse arcs (Fig. S5), formin inhibition or reduced expression of Atn-1 in NIH 3T3 fibroblasts altered the lamellar actin architecture, diminished the intensity of actin bundles, and reduced the size of focal adhesions (Fig. 6, A and B). Similar to U2OS cells, traction stresses were reduced in formin-inhibited NIH 3T3 fibroblasts. However, forces measured in Atn-1 KD NIH 3T3 fibroblasts were indistinguishable from WT 3T3s (Fig. S5).

To identify fibrillar adhesions, immunofluorescence images of tensin and Pxn were obtained simultaneously with phalloidin staining of F-actin using total internal reflection fluorescence (TIRF) microscopy (Fig. 6 A). Tensin-rich plaques that colocalized with Pxn were observed in 73% of the WT cells (n = 15 cells). Strikingly, in both the Dia-inhibited and Atn-1 KD fibroblasts, little to no staining of tensin could be seen in Pxn-rich plaques (Dia Inh, n = 14 cells; Atn-1 KD, n = 17 cells).

To visualize fibronectin remodeling, fibroblasts were plated on fibronectin-coated coverslips for 18 h, and fibronectin was subsequently visualized by immunofluorescence. In WT cells, 100% of cells (n = 23 cells) showed, to varying extents, effects of fibronectin remodeling underneath or nearby the cell (Fig. 6 B). In contrast, only 15% of the formin-inhibited or Atn-1 KD cells exhibited any indication of fibronectin remodeling (Dia Inh, n = 13 cells; Atn-1 KD, n = 19 cells). Thus, even in the presence of strong lamellar contractility and tension on the ECM, fibrillar adhesions required for fibronectin remodeling were eliminated in the formin-inhibited and Atn-1 KD cells. These results underscore the physiological importance of RSF assembly in promoting focal adhesion maturation required to form the tensin-rich fibrillar adhesions used in ECM remodeling.

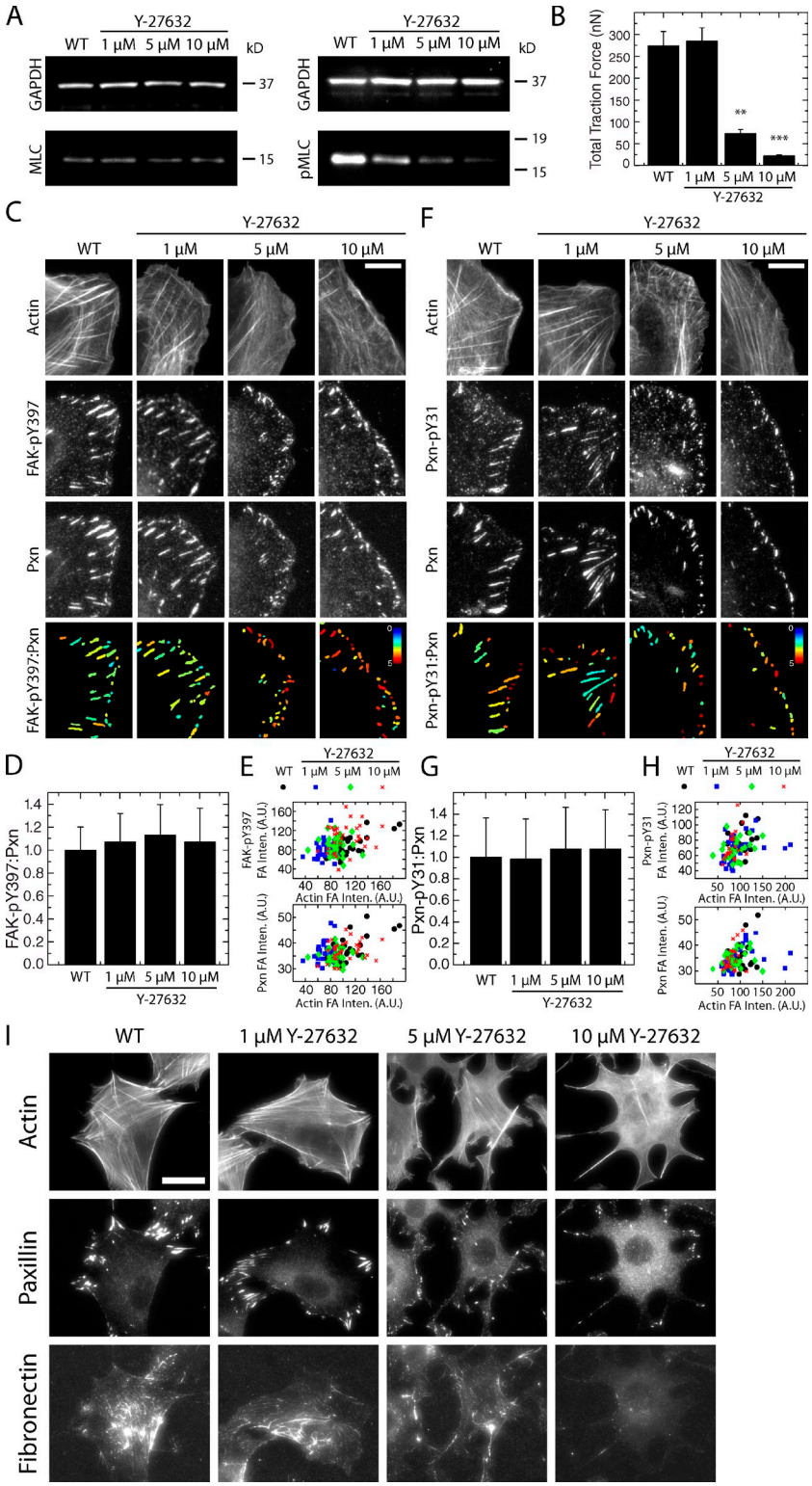

Figure 7. **Composition maturation of focal adhesions and matrix remodeling occurs when cellular tension is reduced by 80%.** (A) Western blot showing reduced levels of pMLC in U2OS cells in the presence of 1, 5, and 10 µM Y-27632 in comparison with the loading control GAPDH. (B) A bar graph showing the total traction force exerted by U2OS cells (error bars indicate SEM; n = 18, 13, 7, and 9 for WT, 1, 5, and 10 µM of Y-27632, respectively; **, $P < 0.01$; ***, $P < 0.001$ with respect to WT). (C) Immunostaining of actin, phosphorylated FAK (FAK-pY397), and Pxn in U2OS cells treated with varying concentrations of Y-27632. The bottom row represents the mean ratio of the background-subtracted FAK-pY397 to Pxn signal at each focal adhesion. Bar, 10 µm. (D) Bar graph of the mean ratio of FAK-pY397:Pxn for WT, 1, 5, and 10 µM of Y-27632 (error bars indicate SEM; $n > 500$ focal adhesions from at least 10 cells for each condition). (E) The mean intensity (Inten.) of FAK-pY397 or Pxn plotted against the mean intensity of actin at each focal adhesion (FA) for the focal adhesions shown in the bottom row of C. A.U., arbitrary unit. (F) Immunostaining of actin, phosphorylated Pxn (Pxn-pY31), and Pxn in U2OS cells treated with Y-27632. The bottom row represents the mean ratio of the background-subtracted Pxn-pY31 to Pxn signal at each focal adhesion. Bar, 10 µm. (G) Bar graph of the mean ratio of Pxn-pY31:Pxn for WT, 1, 5, and 10 µM of Y-27632 (error bars indicate SEM; $n > 500$ focal adhesions from at least 10 cells for each condition). (H) The mean intensity of Pxn-pY31 or Pxn plotted against the mean intensity of actin at each focal adhesion for the focal adhesions shown in the bottom row of F. (I) Representative immunostained images of actin, Pxn, and fibronectin in 3T3s treated with varying concentrations of Y-27632. Bar, 30 µm.

Adhesion maturation occurs over a large range of cellular tensions

To examine how perturbations to intracellular tension impact focal adhesion maturation and matrix remodeling, we examined focal adhesion maturation and fibronectin remodeling in cells treated with varying concentrations of the Rho kinase inhibitor Y-27632. As the concentration of Y-27632 is increased from 1 to 10 µM, the ratio of pMLC to total MLC, as measured by Western blots of cell lysates, decreases from 70 to 95% of that observed in control cells (Fig. 7 A). In conjunction with the reduction in active myosin II, the total traction force exerted by cells also decreases (Fig. 7 B). Cells treated with 1 µM Y-27632 exert traction forces indistinguishable from WT cells. In the presence of 5 µM Y-27632, the total force is reduced

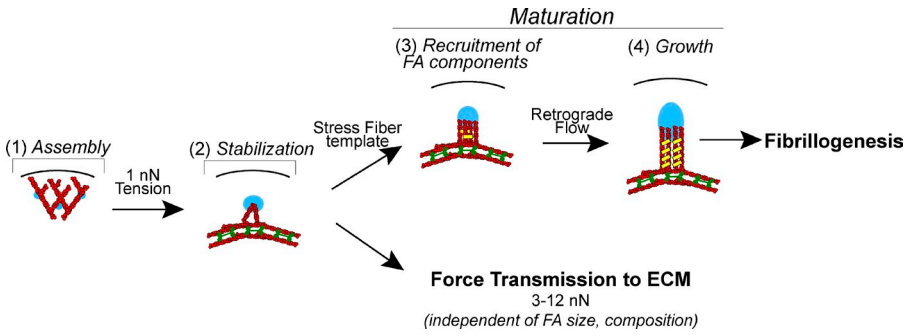

Figure 8. **Distinct roles of actin architecture and tension in focal adhesion maturation.** (1) Nascent adhesions under low tension (0–0.3 nN) assemble in the lamellipodia and turnover on minute time scales. (2) A small amount of tension (~1 nN) generated by myosin II in the lamella stabilizes the adhesions to the ECM. Accumulation of F-actin at the adhesion occurs via an RSF template mediated by Dia1-driven polymerization of F-actin and stabilized by α-actinin cross-linking. (3) The RSF template promotes recruitment of focal adhesion (FA) proteins to facilitate compositional changes. (4) Lamellar retrograde flow drives elongation of the RSF template into an elongated stress fiber as well as adhesion growth. The maturation process that ultimately results in fibrillogenesis can occur over a large range of myosin-generated stresses but is quite sensitive to the actin density at the adhesion plaque. Alternately, compositionally immature adhesions (2) are sufficient to transmit large traction stresses to the ECM, with the stress magnitude dependent on the nature of force transmission in the actin cytoskeleton rather than the size or composition of the adhesion plaque.

to 20% of that exerted by control cells. Traction force exerted by cells treated with 10 µM Y-27632 is ~10% that of control cells. Despite the dramatic reductions in myosin II–generated tension, the recruitment of pY397-FAK and pY31-Pxn to Pxn-rich focal adhesions is not impaired (Fig. 7, C, D, F, and G). Moreover, the density of focal adhesion proteins is directly correlated to the density of F-actin within the focal adhesion plaque (Fig. 7, E and H). Finally, fibronectin remodeling is still observed for cells treated with 5 µM Y-27632 but is almost completely suppressed at 10 µM (Fig. 7 I). Thus, a low threshold of myosin activity is sufficient to facilitate compositional changes characteristic of focal adhesion maturation that results in fibronectin remodeling.

Discussion

Our data identify a crucial role of RSF assembly in myosin-mediated focal adhesion maturation. Nascent adhesions assemble in the lamellipodia (Fig. 8, 1) and, in the absence of myosin activity, turn over rapidly (Choi et al., 2008). Contractile stresses generated by myosin II in lamellar actin networks drive a retrograde frictional slip of nascent adhesions until a tension of 0.9 nN stabilizes the plaques to the ECM (Fig. 8, 2; Aratyn-Schaus and Gardel, 2010). After adhesion stabilization, F-actin density at the adhesion increases via Dia1 assembly of F-actin and subsequent cross-linking into compact bundles via Atn-1 to form an RSF template that promotes further accumulation of focal adhesion proteins and compositional maturation (Fig. 8, 3). A nominal threshold of myosin-generated stress sufficient to drive retrograde flow promotes the elongation of RSFs and focal adhesions (Fig. 8, 4) and, ultimately, facilitates fibrillogenesis.

We find that force transmission to the ECM is surprisingly insensitive to RSF assembly and focal adhesion maturation (Fig. 8). Contractile networks and transverse arcs within the lamella are sufficient to stabilize nascent adhesions into focal adhesions capable of sustaining large tensions on the ECM over physiological time scales. Importantly, the magnitude of traction force is not correlated to focal adhesion size or composition and suggests that force transmission to the ECM is not dominated by properties of focal adhesion plaques but rather the nature of force transmission through the lamellar actomyosin cytoskeleton. Thus, tension at focal adhesions can be regulated independently from their compositional maturation or size, consistent with previous results (Beningo et al., 2001; Stricker et al., 2011).

Our data also show that the presence of stress fibers in the lamellar cytoskeleton is not indicative of the overall contractile or force-generating potential of the cell, consistent with several previous studies (Reinhart-King et al., 2005; Cai et al., 2010; Aratyn-Schaus et al., 2011) and in keeping with the myriad of cellular processes that rely on mechanical forces generated by disordered actomyosin networks and bundles (Gardel et al., 2010; Pollard, 2010; Kasza and Zallen, 2011). Formins play an important role in lamellar F-actin assembly, and we speculate that the reduced density of viable actin filament substrates for myosin motors results in the reduced cellular traction force observed upon Dia inhibition or siRNA Dia1. In contrast, as a promiscuous cross-linker of F-actin, α-actinin may serve to impede the myosin-mediated actin translocation, as has been observed in vitro (Janson et al., 1992). Importantly, we find that disrupting RSF assembly at focal adhesions results in enhanced retrograde flow of the lamellar network, suggesting that RSFs play an important role in both the lamellar viscoelastic resistance and frictional coupling at focal adhesions (Rubinstein et al., 2009). Thus, rather than providing a necessary role in cellular force transmission, stress fibers appear to play important roles in stabilizing the lamellar actin cytoskeleton, providing a scaffold to mediate the maturation of focal adhesions into fibrillar adhesions. This is consistent with the abundance of stress fibers observed during physiological processes involving ECM remodeling (Gutzeit et al., 1991; Haigo and Bilder, 2011).

Thus, force-mediated signals are not sufficient to drive the compositional maturation of focal adhesions. We propose that the dense actin bundle at the adhesion plaque serves a predominately structural role, acting as a stable template to aggregate and cluster adhesion proteins in close proximity and promoting biochemical signaling pathways. Although the mechanism of a lamellar actin template has been proposed before (Chrzanowska-Wodnicka and Burridge, 1996; Choi et al., 2008), previous data were not able to distinguish between the force transmission and adhesion scaffolding roles of RSF architecture.

Our data now show that the lamellar actin architecture can facilitate the recruitment of adhesion proteins and mediate matrix remodeling even when the myosin-mediated tension cues are reduced by 80%. In light of recent ultrastructure data of focal adhesion organization, it will be interesting to explore how various adhesion proteins facilitate transmission of the actin template to integrin-signaling proteins, such as Pxn and FAK, that exist proximal to the plasma membrane (Kanchanawong et al., 2010). Furthermore, it should be noted that our results focus on adhesion formation during protrusion at the cell's leading edge; it will be interesting to explore the consequences of this work for adhesion formation in quiescent cells (Ridley and Hall, 1992; Machesky and Hall, 1997). Importantly, these data provide new insight into the mechanisms underlying myosin-mediated focal adhesion maturation and call into question the extent to which force-dependent pathways dominate this process.

Materials and methods

Cell culture and reagents

U2OS human osteosarcoma cells (American Type Culture Collection) were cultured in McCoy's 5A media (Sigma-Aldrich), and NIH 3T3 mouse fibroblasts (American Type Culture Collection) were cultured in DME media (Mediatech, Inc.). Both were supplemented with 10% FBS (HyClone; Thermo Fisher Scientific), 2 mM L-glutamine (Invitrogen), and penicillin-streptomycin (Invitrogen). U2OS cells were transfected with plasmid DNA constructs encoding for GFP-actin (gifts from the Gary Borisy Laboratory, Northwestern University), mApple-Pxn (a gift from the Mike Davidson Laboratory, Florida State University), and EGFP-Pxn (Laukaitis et al., 2001) using the transfection reagent FuGENE 6 (Roche). The following antibodies were used: mouse anti–α-actinin, mouse anti-fibronectin, mouse anti-MLC, and rabbit anti–pMLC S19 (Sigma-Aldrich); mouse anti–Atn-1 and rabbit anti-tensin (Santa Cruz Biotechnology, Inc.); rabbit anti–FAK-pY397, rabbit anti–Pxn-pY31, and Alexa Fluor 568 goat anti–rabbit (Invitrogen); mouse anti-Pxn (Millipore); Cy5 donkey anti–mouse and Cy2 donkey anti–mouse (Jackson ImmunoResearch Laboratories, Inc.); rabbit anti–pMLC S19 and HRP-linked anti–mouse and anti–rabbit secondary antibodies (Cell Signaling Technology); and mouse anti-FAK (BD). The formin inhibitor SMIFH2 was a gift from D. Kovar (University of Chicago, Chicago, IL; Rizvi et al., 2009) and used at 10–15 µM. Y-27632 was purchased from EMD. Cells were plated for 24 h and then incubated for 45 min in Y-27632 at the concentration indicated for all experiments. For the ECM remodeling in Fig. 7 I, the cells were plated in the presence of the drug.

KD by shRNA and siRNA

shRNA construct sets for human and mouse Atn-1 were purchased from Thermo Fisher Scientific. Transfection of constructs and puromycin selection of expressing cells were performed per the manufacturer's protocols. KD efficiency was determined by Western blotting (Fig. S2), and stable cells lines were maintained for human α-actinin shRNA TRCN0000055825 and mouse α-actinin shRNA TRCN0000090178. ON-TARGETplus SMARTpool siRNA constructs for human Diaph1 were purchased from Thermo Fisher Scientific. The siRNA oligonucleotides and siGLO red transfection indicator were transfected as per the manufacturer's protocol. KD cells selected for analysis had at least four times the background levels of siGLO red.

Western blot analysis

For Western blotting of Atn-1, cells were lysed in radioimmunoprecipitation assay buffer (50 mM Tris, 150 mM NaCl, 0.1% SDS, 0.5% Na deoxycholate, 1% Triton X-100, 1 mM PMSF, and protease inhibitor). Lysates were separated by SDS-PAGE gel and electrotransferred to a nitrocellulose membrane. Blots were blocked in PBS with 5% nonfat dry milk and incubated with primary antibody overnight at 4°C. Blots were incubated in secondary antibody for 1 h at room temperature and developed with ECL Western blotting substrate (Thermo Fisher Scientific). Western blots for MLC and pMLC were performed as per Schneider et al. (2009). Western blots for FAK-pY397, FAK, Pxn-pY31, and Pxn were performed as per Pasapera et al. (2010). Blots were scanned as film negatives on a photo scanner (Perfection v700; Epson) and analyzed using the gel analysis tool in ImageJ (1.44o; National Institutes of Health). The intensity of the protein bands was normalized through comparison with the loading control bands.

Immunofluorescence

Cells were plated on glass coverslips for 24 h before fixation. For ECM remodeling and tensin experiments, coverslips were first incubated with 10 µg/ml fibronectin for 1 h and washed extensively with PBS before plating. For fixation, coverslips were quickly rinsed in cytoskeleton buffer (10 mM MES, 3 mM $MgCl_2$, 1.38 M KCl, and 20 mM EGTA) and then fixed, blocked, and permeabilized in 4% PFA (Electron Microscopy Sciences), 1.5% BSA (Thermo Fisher Scientific), and 0.5% Triton X-100 in cytoskeleton buffer at 37°C for 10 min. Coverslips were washed three times in PBS and incubated with phalloidin (1:1,000) and/or primary antibody (1:400, except anti–Atn-1 [1:100] and antitensin [1:50]) in a blocking solution (1.5% BSA and 0.5% Triton X-100 in cytoskeleton buffer) for at least 1 h at room temperature. After the primary antibody incubation, coverslips were washed three times in PBS and incubated with an appropriate fluorescent secondary antibody (1:1,000) in blocking solution for at least 1 h at room temperature. After the secondary antibody incubation, coverslips were washed in PBS and mounted on glass slides.

PAA substrates for traction force microscopy

PAA substrates containing far-red 40-nm fluorescent microbeads (Invitrogen) were prepared on glass coverslips using previously published methods (Sabass et al., 2008; Aratyn-Schaus et al., 2010). In brief, PAA gels with 7.5%/0.1% and 7.5%/0.3% weight percentages of acrylamide/bis-acrylamide were used to create gels with a shear elastic moduli of 2.8 and 8.6 kPa, respectively (Yeung et al., 2005; Aratyn-Schaus et al., 2010). All traction force measurements of U2OS cells were performed on the 2.8-kPa PAA gels, whereas force measurements of 3T3 cells were performed on the 8.6-kPa PAA gels. Fibronectin (Millipore) was coupled to the surface of the PAA gels by means of sulfo-SANPAH (Thermo Fisher Scientific; Sabass et al., 2008; Aratyn-Schaus and Gardel, 2010; Aratyn-Schaus et al., 2010) or hydrazine hydrate (Aratyn-Schaus et al., 2010; Stricker et al., 2010, 2011), as previously described. In brief, for sulfo-SANPAH coupling, PAA gels were covered with a 2-mg/ml solution of sulfo-SANPAH and exposed to an 8-W UV lamp for ∼2–3 min. The PAA gels were rinsed and incubated with 1 mg/ml fibronectin at room temperature for 1–2 h. The PAA gels were then rinsed repeatedly and plated with cells. For hydrazine coupling, PAA gels were incubated for at least 2 h in undiluted hydrazine followed by a 1-h incubation in 5% acetic acid and then washed. A 10-µg/ml fibronectin solution was prepared in sodium acetate buffer (pH 4.5) and oxidized by an addition of 40 µg/ml sodium metaperiodate before a 30-min incubation on the PAA gel at room temperature. The PAA gels were then rinsed repeatedly and plated with cells.

Microscopy

Live-cell traction force measurements and TIRF immunofluorescence were performed on an inverted microscope (Ti-E; Nikon) with a confocal scanhead (CSUX; Yokogawa Electric Corporation), motorized TIRF illuminator (Nikon), laser merge module containing 491, 561, and 642 laser lines (Spectral Applied Research), and a cooled charge-coupled device camera (HQ2; Roper Scientific). All hardware was controlled via MetaMorph acquisition software (Molecular Devices). Traction force data were obtained at 37°C in a perfusion chamber (Warner Instruments) using a 60× 1.2 NA Plan Apo water immersion objective (Nikon). Cells were maintained in culture media supplemented with 10 mM Hepes and 30 µl/ml Oxyrase (Oxyrase, Inc.).

Immunostained coverslips for TIRF imaging were mounted in PBS on glass slides and sealed with nail polish. All TIRF images were obtained using a 60× 1.49 NA Apo TIRF objective (Nikon). All other immunofluorescence images were collected on an inverted microscope (Ti-E) equipped with a light source (Lumen 200PRO; Prior Scientific) and a cooled charge-coupled device camera (HQ2) and controlled via MetaMorph acquisition software. Coverslips were mounted in ProLong gold (Invitrogen) and sealed with nail polish. Images were obtained using a 40× 1.3 NA Plan Fluor objective (Nikon).

Quantitative immunofluorescence

RSF density (Fig. 1 C) was calculated by counting the number of RSFs per micrometer along a line drawn within the lamella that was parallel to the cell edge. Relative F-actin densities found within RSF and transverse arcs

(Fig. 1 D) were calculated by measuring the mean background-subtracted fluorescence intensities in a region on the RSF and a surrounding region of transverse arcs. Images were taken from a single focal plane in which the lamella was in focus. Ratios of Pxn-pY31:Pxn and FAK-pY397:Pxn (Fig. 5, A, B, D, and E) were determined by thresholding and segmenting the Pxn image to create a mask of the focal adhesions. Using the focal adhesion mask, the background-subtracted intensity was summed in each channel, and the ratio between corresponding image channels was calculated for each adhesion. The ratio images in Fig. 5 (A and D) were created by filling in the mask used to identify the focal adhesions with the mean ratio value for each adhesion. The actin, FAK-pY397, Pxn-pY31, and Pxn intensities in Fig. 5 (C and F) were calculated by taking the mean background-subtracted intensity in each segmented focal adhesion.

Actin flow vectors

Cells were transfected with GFP-actin and plated on a 2.8-kPa PAA gel for live imaging. Images were collected at 30-s intervals for 5–30 min for each cell. Fiducial marks within the lamellar actin were identified and tracked over time using custom software (developed by the Danuser Laboratory, Harvard University, and previously described by Ji and Danuser [2005]). In brief, local intensity maxima were identified and tracked using time-integrated cross-correlations. Templates for the object size for the correlations were adaptively chosen between 0.67 × 0.67 µm and 1.6 × 1.6 µm. Approximately 1,000–3,000 flow vectors were generated for each image. Flow vectors were chosen from regions exhibiting coherent flow ($n > 15$ regions from three to five cells per condition), and the distribution of flow vectors was plotted as box plots.

Displacement analysis and force reconstruction

Methods for traction force microscopy have been previously described (Sabass et al., 2008; Aratyn-Schaus and Gardel, 2010; Stricker et al., 2010). In brief, images of fluorescent beads embedded in the PAA gel were aligned to compensate for experimental drift, and the bead displacement field was calculated between pairs of images by comparing the unstrained bead images obtained after the cell had been removed to images obtained with an attached cell. Displacement fields were calculated using particle imaging velocimetry software in MATLAB (MathWorks), using the minimum quadratic differences algorithm, which calculates the shift necessary to produce the minimum cross-correlation coefficient between a small region of the experiment image and the reference image. Displacement vectors were filtered and interpolated using the kriging interpolation method. We used a displacement grid the size of 0.86 µm for these measurements. From the displacement data, Fourier transform traction cytometry Butler et al., 2002) was then used to estimate traction stress and force at focal adhesions (Sabass et al., 2008). Traction stresses were reconstructed with zeroth-order regularization, which has been shown to yield traction force measurements consistent with the boundary element method (Sabass et al., 2008). Regularization parameters remained constant for all datasets directly compared.

The total traction force exerted by cells (Figs. 3 B, 7 B, and S5) was computed by summing the magnitudes of the traction stress vectors under and near the cell of interest, subtracting the background value (taken from a region outside of the cell, typically around 20 Pa), and multiplying by the area covered by the chosen traction stress vectors.

The distribution of focal adhesion lengths was calculated by thresholding and segmenting focal adhesion images using MATLAB and fitting each adhesion to an ellipse. The length of the adhesion was defined as the major axis of the fitted ellipse. Focal adhesion rates and lifetimes were found by analyzing time-lapse images of focal adhesions by hand to measure the focal adhesion length as a function of time. Focal adhesion lifetimes were determined as the total amount of time a focal adhesion was present in the time lapse. Focal adhesion dynamics were computed by dividing the change in focal adhesion length by the time for assembly and disassembly focal adhesions. Forces at individual focal adhesions were measured by computing the stress at the focal adhesion by interpolating traction stress vectors using a Gaussian weight function and converting the peak stress measured in the adhesion into force by multiplying by the area of the stress footprint at the adhesion (Stricker et al., 2010).

Statistical analysis

To assess statistical significance, we used independent two-sample Student's *t* tests of the mean to determine the significance with respect to WT. The resulting p-values are indicated on the figures and in the figure legends.

Online supplemental material

Fig. S1 shows localization of α-actinin and phosphorylated MLC to stress fibers in a representative immunostained WT U2OS cell. Fig. S2 illustrates the effects of varying the concentration of incubation time of the Dia Inhibitor and shows the Atn-1 KD Western Blots. Fig. S3 shows representative actin immunofluorescence images of WT, Dia Inh, Dia1 siRNA, and Atn-1 KD U2OS cells, as classified and quantified in Fig. 1 C. Fig. S4 shows Western blots and quantification of the relative levels of FAK-pY397:FAK and Pxn-pY31:Pxn, as measured in bulk cell lysates. Fig. S5 shows localization of α-actinin and phosphorylated MLC to stress fibers in a representative immunostained WT 3T3 fibroblast and shows the forces measured for WT, Dia Inh, and Atn-1 KD 3T3 fibroblasts. Video 1 shows the time-lapse images depicted in Fig. 2 D. Video 2 shows the time-lapse images depicted in Fig. 4 B. Online supplemental material is available at http://www.jcb.org/cgi/content/full/jcb.201107042/DC1.

The authors acknowledge the use of computational analysis algorithms to analyze cytoskeletal dynamics and traction forces developed in the laboratories of Gaudenz Danuser and Ulrich Schwarz, respectively.

This work was funded by a Burrough's Wellcome Career Award and National Institutes of Health Director's Pioneer Award (DP10D00354) to M.L. Gardel and by the University of Chicago Materials Research Science and Engineering Center.

Submitted: 7 July 2011
Accepted: 2 January 2012

References

Adelstein, R.S., and M.A. Conti. 1975. Phosphorylation of platelet myosin increases actin-activated myosin ATPase activity. *Nature*. 256:597–598. http://dx.doi.org/10.1038/256597a0

Amano, M., K. Chihara, K. Kimura, Y. Fukata, N. Nakamura, Y. Matsuura, and K. Kaibuchi. 1997. Formation of actin stress fibers and focal adhesions enhanced by Rho-kinase. *Science*. 275:1308–1311. http://dx.doi.org/10.1126/science.275.5304.1308

Aratyn-Schaus, Y., and M.L. Gardel. 2010. Transient frictional slip between integrin and the ECM in focal adhesions under myosin II tension. *Curr. Biol.* 20:1145–1153. http://dx.doi.org/10.1016/j.cub.2010.05.049

Aratyn-Schaus, Y., P.W. Oakes, J. Stricker, S.P. Winter, and M.L. Gardel. 2010. Preparation of complaint matrices for quantifying cellular contraction. *J. Vis. Exp.* 46:e2173.

Aratyn-Schaus, Y., P.W. Oakes, and M.L. Gardel. 2011. Dynamic and structural signatures of lamellar actomyosin force generation. *Mol. Biol. Cell*. 22:1330–1339. http://dx.doi.org/10.1091/mbc.E10-11-0891

Ballestrem, C., N. Erez, J. Kirchner, Z. Kam, A. Bershadsky, and B. Geiger. 2006. Molecular mapping of tyrosine-phosphorylated proteins in focal adhesions using fluorescence resonance energy transfer. *J. Cell Sci.* 119:866–875. http://dx.doi.org/10.1242/jcs.02794

Beningo, K.A., M. Dembo, I. Kaverina, J.V. Small, and Y.L. Wang. 2001. Nascent focal adhesions are responsible for the generation of strong propulsive forces in migrating fibroblasts. *J. Cell Biol.* 153:881–888. http://dx.doi.org/10.1083/jcb.153.4.881

Burnette, D.T., S. Manley, P. Sengupta, R. Sougrat, M.W. Davidson, B. Kachar, and J. Lippincott-Schwartz. 2011. A role for actin arcs in the leading-edge advance of migrating cells. *Nat. Cell Biol.* 13:371–381. http://dx.doi.org/10.1038/ncb2205

Butler, J.P., I.M. Tolić-Nørrelykke, B. Fabry, and J.J. Fredberg. 2002. Traction fields, moments, and strain energy that cells exert on their surroundings. *Am. J. Physiol. Cell Physiol.* 282:C595–C605.

Cai, Y., O. Rossier, N.C. Gauthier, N. Biais, M.-A. Fardin, X. Zhang, L.W. Miller, B. Ladoux, V.W. Cornish, and M.P. Sheetz. 2010. Cytoskeletal coherence requires myosin-IIA contractility. *J. Cell Sci.* 123:413–423. http://dx.doi.org/10.1242/jcs.058297

Campellone, K.G., and M.D. Welch. 2010. A nucleator arms race: Cellular control of actin assembly. *Nat. Rev. Mol. Cell Biol.* 11:237–251. http://dx.doi.org/10.1038/nrm2867

Choi, C.K., M. Vicente-Manzanares, J. Zareno, L.A. Whitmore, A. Mogilner, and A.R. Horwitz. 2008. Actin and alpha-actinin orchestrate the assembly and maturation of nascent adhesions in a myosin II motor-independent manner. *Nat. Cell Biol.* 10:1039–1050. http://dx.doi.org/10.1038/ncb1763

Chrzanowska-Wodnicka, M., and K. Burridge. 1996. Rho-stimulated contractility drives the formation of stress fibers and focal adhesions. *J. Cell Biol.* 133:1403–1415. http://dx.doi.org/10.1083/jcb.133.6.1403

Danuser, G., and C.M. Waterman-Storer. 2006. Quantitative fluorescent speckle microscopy of cytoskeleton dynamics. *Annu. Rev. Biophys. Biomol. Struct.* 35:361–387. http://dx.doi.org/10.1146/annurev.biophys.35.040405.102114

Forscher, P., and S.J. Smith. 1988. Actions of cytochalasins on the organization of actin filaments and microtubules in a neuronal growth cone. *J. Cell Biol.* 107:1505–1516. http://dx.doi.org/10.1083/jcb.107.4.1505

Gardel, M.L., I.C. Schneider, Y. Aratyn-Schaus, and C.M. Waterman. 2010. Mechanical integration of actin and adhesion dynamics in cell migration. *Annu. Rev. Cell Dev. Biol.* 26:315–333. http://dx.doi.org/10.1146/annurev.cellbio.011209.122036

Geiger, B., and K.M. Yamada. 2011. Molecular architecture and function of matrix adhesions. *Cold Spring Harb. Perspect. Biol.* 3:a005033. http://dx.doi.org/10.1101/cshperspect.a005033

Geiger, B., J.P. Spatz, and A.D. Bershadsky. 2009. Environmental sensing through focal adhesions. *Nat. Rev. Mol. Cell Biol.* 10:21–33. http://dx.doi.org/10.1038/nrm2593

Gupton, S.L., K. Eisenmann, A.S. Alberts, and C.M. Waterman-Storer. 2007. mDia2 regulates actin and focal adhesion dynamics and organization in the lamella for efficient epithelial cell migration. *J. Cell Sci.* 120:3475–3487. http://dx.doi.org/10.1242/jcs.006049

Gutzeit, H.O., W. Eberhardt, and E. Gratwohl. 1991. Laminin and basement membrane-associated microfilaments in wild-type and mutant *Drosophila* ovarian follicles. *J. Cell Sci.* 100:781–788.

Haigo, S.L., and D. Bilder. 2011. Global tissue revolutions in a morphogenetic movement controlling elongation. *Science*. 331:1071–1074. http://dx.doi.org/10.1126/science.1199424

Heath, J.P. 1983. Behaviour and structure of the leading lamella in moving fibroblasts. I. Occurrence and centripetal movement of arc-shaped microfilament bundles beneath the dorsal cell surface. *J. Cell Sci.* 60:331–354.

Hotulainen, P., and P. Lappalainen. 2006. Stress fibers are generated by two distinct actin assembly mechanisms in motile cells. *J. Cell Biol.* 173:383–394. http://dx.doi.org/10.1083/jcb.200511093

Janson, L.W., J.R. Sellers, and D.L. Taylor. 1992. Actin-binding proteins regulate the work performed by myosin II motors on single actin filaments. *Cell Motil. Cytoskeleton*. 22:274–280. http://dx.doi.org/10.1002/cm.970220407

Ji, L., and G. Danuser. 2005. Tracking quasi-stationary flow of weak fluorescent signals by adaptive multi-frame correlation. *J. Microsc.* 220:150–167. http://dx.doi.org/10.1111/j.1365-2818.2005.01522.x

Kanchanawong, P., G. Shtengel, A.M. Pasapera, E.B. Ramko, M.W. Davidson, H.F. Hess, and C.M. Waterman. 2010. Nanoscale architecture of integrin-based cell adhesions. *Nature*. 468:580–584. http://dx.doi.org/10.1038/nature09621

Kasza, K.E., and J.A. Zallen. 2011. Dynamics and regulation of contractile actin-myosin networks in morphogenesis. *Curr. Opin. Cell Biol.* 23:30–38. http://dx.doi.org/10.1016/j.ceb.2010.10.014

Koestler, S.A., S. Auinger, M. Vinzenz, K. Rottner, and J.V. Small. 2008. Differentially oriented populations of actin filaments generated in lamellipodia collaborate in pushing and pausing at the cell front. *Nat. Cell Biol.* 10:306–313. http://dx.doi.org/10.1038/ncb1692

Laukaitis, C.M., D.J. Webb, K. Donais, and A.F. Horwitz. 2001. Differential dynamics of α5 integrin, paxillin, and α-actinin during formation and disassembly of adhesions in migrating cells. *J. Cell Biol.* 153:1427–1440. http://dx.doi.org/10.1083/jcb.153.7.1427

Machesky, L.M., and A. Hall. 1997. Role of actin polymerization and adhesion to extracellular matrix in Rac- and Rho-induced cytoskeletal reorganization. *J. Cell Biol.* 138:913–926. http://dx.doi.org/10.1083/jcb.138.4.913

Pankov, R., E. Cukierman, B.Z. Katz, K. Matsumoto, D.C. Lin, S. Lin, C. Hahn, and K.M. Yamada. 2000. Integrin dynamics and matrix assembly: Tensin-dependent translocation of $\alpha_5\beta_1$ integrins promotes early fibronectin fibrillogenesis. *J. Cell Biol.* 148:1075–1090. http://dx.doi.org/10.1083/jcb.148.5.1075

Parsons, J.T., A.R. Horwitz, and M.A. Schwartz. 2010. Cell adhesion: Integrating cytoskeletal dynamics and cellular tension. *Nat. Rev. Mol. Cell Biol.* 11:633–643. http://dx.doi.org/10.1038/nrm2957

Pasapera, A.M., I.C. Schneider, E. Rericha, D.D. Schlaepfer, and C.M. Waterman. 2010. Myosin II activity regulates vinculin recruitment to focal adhesions through FAK-mediated paxillin phosphorylation. *J. Cell Biol.* 188:877–890. http://dx.doi.org/10.1083/jcb.200906012

Peterson, L.J., Z. Rajfur, A.S. Maddox, C.D. Freel, Y. Chen, M. Edlund, C. Otey, and K. Burridge. 2004. Simultaneous stretching and contraction of stress fibers in vivo. *Mol. Biol. Cell*. 15:3497–3508. http://dx.doi.org/10.1091/mbc.E03-09-0696

Pollard, T.D. 2010. Mechanics of cytokinesis in eukaryotes. *Curr. Opin. Cell Biol.* 22:50–56. http://dx.doi.org/10.1016/j.ceb.2009.11.010

Reinhart-King, C.A., M. Dembo, and D.A. Hammer. 2005. The dynamics and mechanics of endothelial cell spreading. *Biophys. J.* 89:676–689. http://dx.doi.org/10.1529/biophysj.104.054320

Ridley, A.J., and A. Hall. 1992. The small GTP-binding protein rho regulates the assembly of focal adhesions and actin stress fibers in response to growth factors. *Cell*. 70:389–399. http://dx.doi.org/10.1016/0092-8674(92)90163-7

Riveline, D., E. Zamir, N.Q. Balaban, U.S. Schwarz, T. Ishizaki, S. Narumiya, Z. Kam, B. Geiger, and A.D. Bershadsky. 2001. Focal contacts as mechanosensors: Externally applied local mechanical force induces growth of focal contacts by an mDia1-dependent and ROCK-independent mechanism. *J. Cell Biol.* 153:1175–1186. http://dx.doi.org/10.1083/jcb.153.6.1175

Rizvi, S.A., E.M. Neidt, J. Cui, Z. Feiger, C.T. Skau, M.L. Gardel, S.A. Kozmin, and D.R. Kovar. 2009. Identification and characterization of a small molecule inhibitor of formin-mediated actin assembly. *Chem. Biol.* 16:1158–1168. http://dx.doi.org/10.1016/j.chembiol.2009.10.006

Rubinstein, B., M.F. Fournier, K. Jacobson, A.B. Verkhovsky, and A. Mogilner. 2009. Actin-myosin viscoelastic flow in the keratocyte lamellipod. *Biophys. J.* 97:1853–1863. http://dx.doi.org/10.1016/j.bpj.2009.07.020

Sabass, B., M.L. Gardel, C.M. Waterman, and U.S. Schwarz. 2008. High resolution traction force microscopy based on experimental and computational advances. *Biophys. J.* 94:207–220. http://dx.doi.org/10.1529/biophysj.107.113670

Schneider, I.C., C.K. Hays, and C.M. Waterman. 2009. Epidermal growth factor-induced contraction regulates paxillin phosphorylation to temporally separate traction generation from de-adhesion. *Mol. Biol. Cell*. 20:3155–3167. http://dx.doi.org/10.1091/mbc.E09-03-0219

Schwartz, M.A. 2010. Integrins and extracellular matrix in mechanotransduction. *Cold Spring Harb. Perspect. Biol.* 2:a005066. http://dx.doi.org/10.1101/cshperspect.a005066

Shi, Q., and D. Boettiger. 2003. A novel mode for integrin-mediated signaling: Tethering is required for phosphorylation of FAK Y397. *Mol. Biol. Cell*. 14:4306–4315. http://dx.doi.org/10.1091/mbc.E03-01-0046

Stricker, J., B. Sabass, U.S. Schwarz, and M.L. Gardel. 2010. Optimization of traction force microscopy for micron-sized focal adhesions. *J. Phys. Condens. Matter*. 22:194104. http://dx.doi.org/10.1088/0953-8984/22/19/194104

Stricker, J., Y. Aratyn-Schaus, P.W. Oakes, and M.L. Gardel. 2011. Spatiotemporal constraints on the force-dependent growth of focal adhesions. *Biophys. J.* 100:2883–2893. http://dx.doi.org/10.1016/j.bpj.2011.05.023

Vogel, V., and M. Sheetz. 2006. Local force and geometry sensing regulate cell functions. *Nat. Rev. Mol. Cell Biol.* 7:265–275. http://dx.doi.org/10.1038/nrm1890

Webb, D.J., K. Donais, L.A. Whitmore, S.M. Thomas, C.E. Turner, J.T. Parsons, and A.F. Horwitz. 2004. FAK-Src signalling through paxillin, ERK and MLCK regulates adhesion disassembly. *Nat. Cell Biol.* 6:154–161. http://dx.doi.org/10.1038/ncb1094

Yeung, T., P.C. Georges, L.A. Flanagan, B. Marg, M. Ortiz, M. Funaki, N. Zahir, W. Ming, V. Weaver, and P.A. Janmey. 2005. Effects of substrate stiffness on cell morphology, cytoskeletal structure, and adhesion. *Cell Motil. Cytoskeleton*. 60:24–34. http://dx.doi.org/10.1002/cm.20041

Zaidel-Bar, R., R. Milo, Z. Kam, and B. Geiger. 2007. A paxillin tyrosine phosphorylation switch regulates the assembly and form of cell-matrix adhesions. *J. Cell Sci.* 120:137–148. http://dx.doi.org/10.1242/jcs.03314